Carrier Mobility Dominated Gas-Sensing: A Room-Temperature Gas-Sensing Mode for SnO_2 Nanorod Array Sensors

*Shipu Xu, Huaping Zhao, Yang Xu, Rui Xu, Yong Lei**

Institute für Physik & IMN MacroNano (ZIK), Technische Universität Ilmenau, Ilmenau 98693, Germany

KEYWORDS: gas-sensing modes, inorganic semiconductors, carrier mobility, room temperature, nanorod arrays

ABSTRACT: Adsorption-induced changing of carrier density is presently dominating inorganic semiconductor gas-sensing, which is usually operated at a high temperature. Besides carrier density, other carrier characteristics might also play a critical role for gas-sensing. Here we show that carrier mobility can be an efficient parameter to dominate gas sensing, by which room temperature gas-sensing of inorganic semiconductors is realized *via* a carrier mobility dominated gas-sensing (CMDGS) mode. To demonstrate the CMDGS, we design and prepare a gas-sensor based on a regular array of SnO_2 nanorods on a bottom film. It is found that a key for determining gas sensing mode is adjusting the length of the arrayed nanorods. With the nanorod length changing from 340 to 40 nm, the gas sensing behavior changes from the conventional carrier-density mode to a complete carrier-mobility mode. Moreover, comparing to the carrier

density dominating gas-sensing, the proposed CMDGS mode enhances the sensor sensitivity. The CMDGS proves an emerging gas-sensing mode for designing inorganic semiconductor gas-sensors with high performances at room temperature.

1. INTRODUCTION

Inorganic semiconductor gas-sensors are most wildly-used solid-state gas-sensors owing to their high sensitivity, fast-response time, and high chemical stability.[1-5] Development of inorganic semiconductor gas-sensors is dependent on gas-sensing modes, among which the dominant gas-sensing mode relies on a fact that surface adsorption on inorganic semiconductors can influence their carrier density to vary the conductivity.[6-8] The surface adsorption origin of the carrier density variation is the key to this dominant gas-sensing mode, which is therefore denoted as 'carrier density dominated gas-sensing' (CDDGS) in the following description. Operating the CDDGS needs a high temperature. For example, the operating temperature for a SnO_2 gas-sensor is usually higher than 200 ºC,[7] which may cause tedious operations, over-consumptions of energy, and even some safety issues when such a CDDGS-mode gas-sensor is employed.

Besides carrier density, other crucial carrier characteristics of gas-sensing materials such as carrier mobility might also play a key role for gas sensing.[9-12] It has been shown that hydrogen detection using platinum nanowires is related to adsorption-induced degradation of carrier mobility.[9,10] Actually, a similar adsorption-origin of the carrier mobility degradation also exists in inorganic semiconductor gas-sensing, but only being limited on the surface.[5,13] In the case of the oxygen adsorption on the SnO_2 film,[13] an oxygen molecule is adsorbed and forms a scattering center on the surface of SnO_2. This scattering center radiates a spherical region with Debye length (*ca.* 3 nm), and carrier mobility is distinctly diminished within this region. This region can

completely occupy the carrier channel as the thickness of the SnO_2 film decreases to 2-times Debye length, generating a carrier mobility degradation for most carriers. Recently, the adsorption-induced degradation of carrier-mobility has also occurred when using a 4.8-nm-thin phosphorene nanosheet to detect NO_2 gas.[5] The 4.8 nm thickness of the phosphorene nanosheet causes that the adsorbed NO_2 molecules can directly diminish the carrier mobility through the carrier channel. The resulting degradation of carrier mobility is positively associated with the concentration of NO_2 gas. However, limited by the low surface area of the above-mentioned platforms (*e.g.*, the SnO_2 film and the phosphorene nanosheet), the adsorbed quantity of the oxygen molecule or the NO_2 molecule is still far from achieving a carrier mobility degradation which is large enough to produce an obvious variation of conductivity, and consequently so far such carrier mobility degradation has not been utilized to dominate gas-sensing of inorganic semiconductors.

Based on these recognitions and considering a fact that carrier mobility has a positive correlation with the conductivity of inorganic semiconductors, it shall be worthy to explore a concept of carrier mobility dominated gas-sensing (CMDGS) as an alternative gas-sensing mode of inorganic semiconductors. Here we design a gas-sensing configuration of inorganic semiconductors to realize the CMDGS, aiming room-temperature gas-sensing. This design involves two key points: (i) vertically aligned nanorods and (ii) a bottom film. The inter-electrode bottom film specifically serves as a conductive channel, and the carrier mobility within the channel could be modulated by a large adsorption on the nanorods.

As a proof-of-concept, SnO_2, a traditional inorganic semiconductor for gas-sensing,[14-17] is chosen as a model material; and an ultrathin alumina membrane (UTAM)[18-20] is applied as a template. Regular arrays of SnO_2 nanorods on a bottom film are then fabricated with different nanorod

lengths (340, 140, 110, and 40 nm), which are used to construct a room temperature gas sensor. It is found that, when the nanorod length decreases from 340 to 40 nm, the gas-sensing mode changes from the carrier density dominated gas-sensing (*i.e.*, CDDGS) to carrier mobility dominated gas-sensing (*i.e.*, CMDGS). For the 340-nm-length nanorod array, its gas sensing still stays in CDDGS, while the CMDGS mode appears for the 140-nm-length nanorod together with CDDGS. With further decreasing of nanorod length, the CMDGS becomes obvious for the 110-nm-length nanorod array, and finally the gas sensing of the 40-nm-length nanorod is completely in the CMDGS range. Importantly, the CMDGS-mode sensor (*i.e.*, 40-nm-length nanorod array) shows a more than 4-times higher sensitivity compared to that of the CDDGS-mode sensor. To fully understand the mechanism of the changing from CDDGS to CMDGS mode, two representative SnO_2 nanorod arrays (40 and 340 nm nanorod lengths) are fabricated into field-effect transistors. For all three target gases of ethanol, acetone, and isopropanol, electric characterizations of the field-effect transistors show that the carrier mobility of the 40-nm-length nanorod array decreases for more than 90% after introducing gases. Together with the morphological origin of electric field distributions, a large adsorption-induced degradation of carrier mobility is demonstrated for the 40-nm-length nanorod array, endowing it with sensitive responses of CMDGS at room temperature. Based on the above, the proposed CMDGS is confirmed as an efficient gas-sensing mode for obtaining a room temperature gas sensor with high sensitivity.

2. EXPERIMENTAL SECTION

2.1. Synthesis of UTAMs. UTAMs were synthesized from high purity aluminum (Al) foils by a two-step anodization process. This anodization process included a 6-hour-first and a short-time-second anodization, at 40 V in 0.3 M oxalic acid. The second anodization was conducted at 2 ºC.

The UTAMs with 80, 110, 140, and 340 nm of thicknesses can be respectively obtained by 2, 3, 5, and 10 minutes of the second anodization. Next the samples were correspondingly transferred into a 5 wt% H_3PO_4 solution at 30 ºC for 4, 8, 15, and 25 minutes to widen the pore diameter up to 60 nm. A polymethylmethacrylate (PMMA) layer formed by 6% PMMA/Chlorobenzene solution was subsequently deposited on the top of the Al layer to support the UTAM. The Al layer on the backside of the UTAM/PMMA was removed in a mixture solution of $CuCl_2$ and HCl. With the aid of a plastic strainer, the UTAM/PMMA was transferred in the H_3PO_4 solution at 30 ºC for 14 minutes to remove the barrier of the UTAM. After removal of the PMMA in acetone, the UTAM with uniform opened pores was obtained.

2.2. Fabrication of SnO_2 nanorod arrays. Different weights of $SnCl_4$ were dissolved in deionized water to form homogeneous transparent solutions with different concentrations, ranging from 0.01 to 0. 1 M. Herein, the 0.1M and the 0.01 M $SnCl_4$ aqueous solution represented the high and the low concentration precursor solution, and were used for the fabrications of the long (*i.e.*, 340, 140, and 110 nm nanorod length) and the short (*i.e.*, 40 nm nanorod length) SnO_2 nanorod array. As shown in Figure 2a, a UTAM was slowly immersed into a $SnCl_4$ aqueous solution, and then it was floated onto the surface of the solution. Subsequently, this floated template was picked up with a device substrate. Next the sample was annealed using a heat-treatment process normally for achieving nanocomposites or nanoparticles,[21,22] in a furnace with a first hot plate at 150 ºC for 2 hours and an immediate second hot plate at 450 ºC for 2 hours. Finally, the SnO_2 nanorod array was obtained after the removal of the UTAM in a H_3PO_4 solution (5 wt%).

2.3. Gas-sensing tests. Gas-sensing tests were conducted in an air-tight chamber with electrical feedthroughs. A constant voltage of 4 V was applied to a device and the variation of the output

current was monitored and recorded with the change in the gas environment using a Keithley semiconducting testing system. The reducing gases (25 ppm of ethanol, propanol, and acetone gases) were respectively chosen as a target gas. A typical gas-sensing measurement consists of three sequential steps: (1) a base value of the output current from the sensor in air was recorded; (2) a calculated volume of the reducing gas was introduced into a chamber, and the signal on the variation of output current was simultaneously recorded; (3) after the signal stabilized, the chamber was opened for removing the gas, and the signal of the output current was also simultaneously recorded until it reached a steady state. Characterizations of the field-effect transistor were also conducted by this sensing system.

2.4. Characterizations. The morphology of SnO_2 nanorod arrays on device substrates was examined by scanning electron microscopy (SEM, S4800 Hitachi and Quanta 250 FEG). The compositions were characterized by X-ray diffraction (XRD, D/max2200, with Cu-Ka radiation) and X-ray photoelectron spectroscopy (XPS, ESCALAB 250). Samples for these measurements were prepared on silicon (Si) substrates under the same conditions as those prepared on the device substrate. For preparing the specimens of transmission electron microscopy (TEM), the SnO_2 nanorod array was scraped off and transferred onto carbon-coated transmission electron microscopy grids. A JEOL JEM 2010 transition electronic microscope was used for the TEM analysis.

3. RESULTS AND DISCUSSION

3.1. Simulated electric field of the SnO_2 nanorod array and its CMDGS mode. To reveal a possibility of the CMDGS mode based on the designed SnO_2 nanorod array, we perform a simulation of electric field on the SnO_2 nanorod array and a comparison to that of a SnO_2 film.

Figure 1a and b show cross-sectional electric field distributions of a SnO_2 film and the SnO_2 nanorod array, respectively. In Supporting Information S1, we present the electric field strengths on the surfaces of the SnO_2 film and the bottom film of the nanorod array (both arrowed in red color in Figure 1a and b). It is shown that, a higher electric field strength exists on the surface of bottom film (more than 0.49×10^6 V/m) rather than that of the film (0.4×10^6 V/m), meaning more cumulative charges (*i.e.*, carrier). Considering the bottom film of the SnO_2 nanorod array is specifically designed to be a conductive channel, the adsorption on the bottom film surface therefore has a higher possibility to induce carrier scattering. As a valid supporting, a high electric field strength of more than 0.49×10^6 V/m is also confirmed to exist on the bottom film surfaces of the nanorod arrays with nanorod lengths ranging from 20 to 340 nm (see Supporting Information S1). Additionally, the vertical nanorods shall introduce a larger surface adsorption for the SnO_2 nanorod array and cover the shortage aroused by the SnO_2 degraded room-temperature ability of adsorption, as portrayed in Figure 1c and d. These results indicate that the gas-sensing of the SnO_2 nanorod array could be subjected to a larger adsorption-induced degradation of carrier mobility than that of the SnO_2 film. Hence, it is highly possible that the SnO_2 nanorod array can exhibit a CMDGS response. As shown in Figure 1c and d, the CMDGS of the SnO_2 nanorod array with the large adsorption-induced degradation of carrier mobility would manifest as a more obvious decrease of current intensity (Figure 1d) than that of the SnO_2 film (Figure 1c).

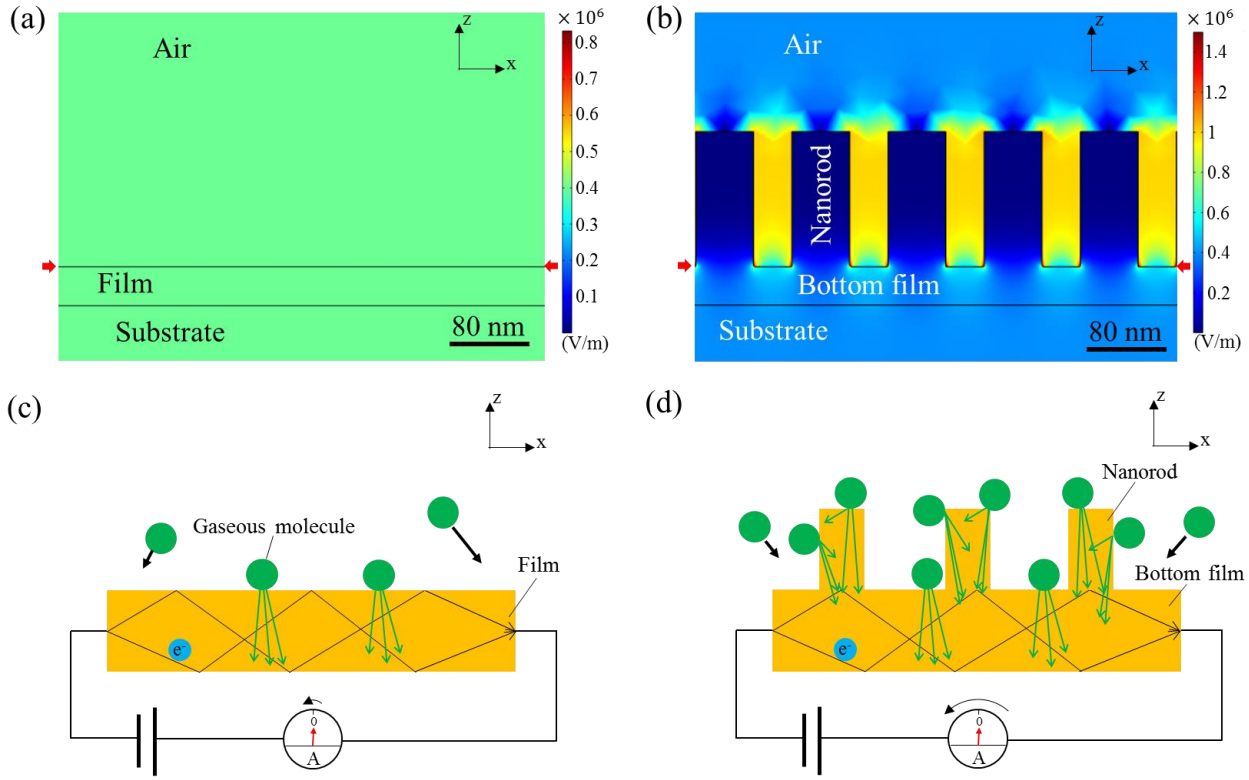

Figure 1. (a and b) Electric fields of the SnO_2 film (a) and the SnO_2 nanorod array (b) in air. (c and d) Schematics of gas-sensing responses (*i.e.*, current variation) of the SnO_2 film (c) and the SnO_2 nanorod array (d). Applied with a constant voltage, the SnO_2 nanorod array with a large adsorption-induced degradation of carrier mobility would exhibit a more obvious current decrease than that of the SnO_2 film, reflecting a distinct CMDGS response.

3.2. Fabrication of SnO_2 nanorod arrays on device substrates. For the designed configuration of SnO_2 nanorod array gas-sensors, the key point is that the bottom film bridging over two sensor electrodes serves as a conductive channel. Then a UTAM-based fabrication of SnO_2 nanorod arrays is used and schematically illustrated in Figure 2a. The UTAM (its morphology shown in Figure S2, Supporting Information) was firstly immersed into precursor solution of SnO_2 (Figure $2a_1$), then floated on the surface of solution (Figure $2a_2$). The solution filled each channel of the

UTAM due to the capillary effect.[23] Next this floated UTAM was picked up by a device substrate (Figure 2a$_3$). For the construction of the device substrate, interdigitated platinum/titanium (Pt/Ti) electrodes were seated on a substrate, a p-type Si substrate capped with a 300-nm-thick oxide layer. The UTAM covered the surface of the device substrate with the solution permeating its channels and bottom interval (Figure 2a$_4$). The existence of the bottom interval enabled the following growth of the bottom film on the device substrate, as depicted in the magnified image of Figure 2a$_4$. Then a heating measurement was performed on this sample (Figure 2a$_5$), resulting in the vertical SnO_2 nanorods in the UTAM channels and the bottom film in the bottom interval, of which SEM image is shown in Figure 2b. Finally, the SnO_2 nanorod array gas-sensor was obtained after the removal of the UTAM in an aqueous H_3PO_4 solution (Figure 2a$_6$, its SEM images shown in Figure S3, Supporting Information). The sample composition is characterized by TEM, XRD, and XPS (see Supporting Information S4 and S5).

Using the above-mentioned UTAM-based technique, we prepare SnO_2 nanorod arrays with different lengths ranging from 340 to 40 nm (more details about the fabrication are available in Supporting Information S6-S8). In a plane view of the SnO_2 nanorod array (Figure 2c), its SEM image depicts that nanorods are vertically and hexagonally arranged with a period of 100 nm. In cross-section views, different lengths of the nanorods can be observed, such as 340 nm (the upper part of Figure 2d), 140 nm (the upper part of Figure 2e), 110 nm (the lower part of Figure 2e), and 40 nm (the lower part of Figure 2d). Additionally, a 40-nm-thick bottom film can be clearly found in the 340 nm sample (the upper part of Figure 2d). Both arrays are of the same density of nanorods, which is characterized by the same period and nanorod diameter (*i.e.*, 100 nm and 60 nm). Then we use these nanorod arrays as a gas-sensor for following measurements.

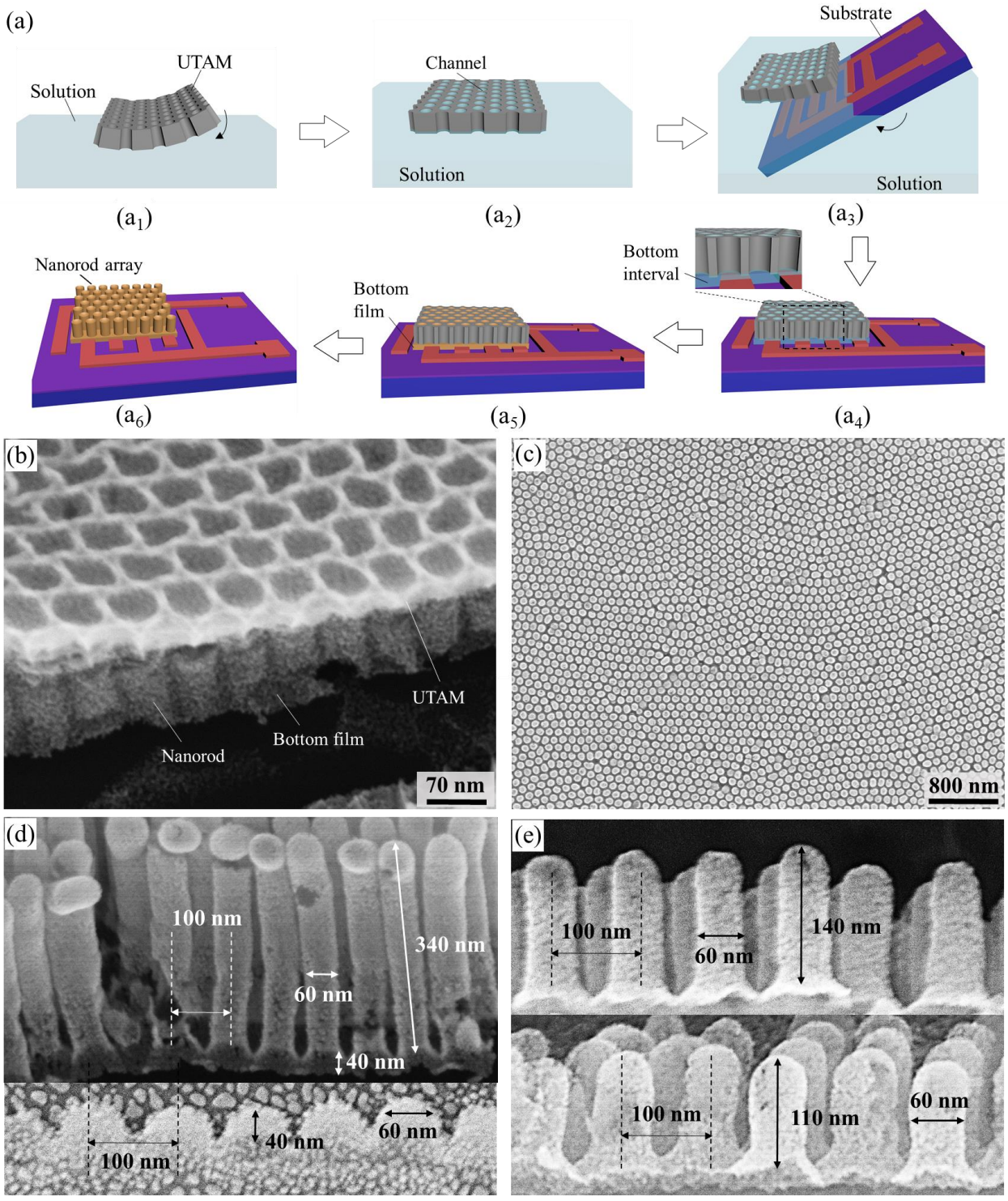

Figure 2. The SnO_2 nanorod array gas-sensor fabrication. (a) The schematic representation of procedures for fabricating the SnO_2 nanorod array on a device substrate: (a_1) transferring a

UTAM to the precursor solution; (a_2) the UTAM floated on the precursor solution; (a_3) picking up the UTAM with a device substrate; (a_4) the UTAM covering on the device substrate, the magnified image of the selected area showing the solution permeates the UTAM channels and bottom interval; (a_5) drying and annealing both the UTAM and the device substrate; (a_6) the SnO_2 nanorod array obtained after the removal of the UTAM. (b) A SEM image showing the SnO_2 nanorod array without the removal of the UTAM. (c) A plane view of the SnO_2 nanorod array. (d and e) Cross-section views of the SnO_2 nanorod arrays with different nanorod lengths, involving 340 nm (the upper part of d), 40 nm (the lower part of d), 140 nm (the upper part of e), and 110 nm (the lower part of e). An obvious 40-nm-thick bottom film is observed from the 340-nm-length nanorod array (the upper part of d).

3.3. Gas-sensing of SnO_2 nanorod arrays. In our gas-sensing measurements, applied with a constant voltage of 4 V, changes of I_t/I_0 value from gas-sensors on exposure to detected gases are monitored and recorded as sensing signals.[15,24] I_0 and I_t are output currents of a sensor in air and detected atmospheres, respectively. Detected gases involve 25 ppm of ethanol, isopropanol, and acetone gas. Figure 3a-d show room temperature gas-sensing responses of SnO_2 nanorod arrays consisting of different nanorod lengths (340, 140, 110, and 40 nm). It can be seen that the positive gas-sensing response ($I_t/I_0 > 1$) turns negative ($I_t/I_0 < 1$) when the nanorod length decreases from 340 to 40 nm. As the SnO_2 nanorod array is applied with a constant voltage, a positive and a negative gas-sensing response indicate an increase and a decrease of sample conductivity respectively after the introduction of detected gases. Figure 3a describes the conductivity of the 340-nm-length SnO_2 nanorod array increases after the introduction of detected gases. All the detected gases (ethanol, isopropanol, and acetone gases) are reducing gases those can react with the oxygen ions (O^{2-} and O^-) on SnO_2 surface, resulting in releasing of

trapped electrons.[25] As the SnO_2 nanorod arrays (*e.g.*, the 340 nm and the 40 nm sample) behave as a n-type conductance channel (Supporting Information S9), the releasing of trapped electrons from the oxygen ions to SnO_2 increases the carrier density in the SnO_2 nanorod array, therefore increasing the SnO_2 conductivity. It suggests that the positive gas-sensing response of 340-nm-length SnO_2 nanorod array is a typical CDDGS response. In the detection of 25 ppm acetone gas, this sample exhibits a gas-sensing response with the I_t/I_0 of 1.13. However, this response to the acetone gas becomes weak ($I_t/I_0 \sim 0$) when the nanorod length decreases to 140 nm (Figure 3b), and then turns to an unusual negative ($I_t/I_0 = 0.93$) response as the length of nanorod continuously decreases to 110 nm (Figure 3c). This kind of negative gas-sensing response indicates that, for the 110-nm-length SnO_2 nanorod sample, the introduction of the acetone gas doesn't increase the conductivity but rather decreases it. Considering that the sample conductivity (σ) is a product of carrier density and mobility (*i.e.*, $\sigma = nq\mu$, n, q, and μ are carrier density, carrier charge, and carrier mobility), this conductivity decreasing could be only caused by the decrease in carrier density and/or the degradation of carrier mobility. The aforementioned fact confirms that reducing gases (*e.g.*, acetone gas) always lead to the carrier density increase in the SnO_2 nanorod arrays, and thus the conductivity decreasing of the 110-nm-length SnO_2 nanorod array shall be attributed to a large degradation of carrier mobility. When the nanorod length further decreases to such as 40 nm (Figure 3d), this negative gas-sensing response caused by the degradation of carrier mobility becomes more distinct, revealing that a carrier mobility dominated gas-sensing (*i.e.*, CMDGS) mode dominates the gas-sensing when the nanorod length is 40 nm. Additionally, it further demonstrates the CMDGS in the 40 nm sample that the negative responses exist on the samples with different nanorod diameters (see Supporting Information S10). Importantly, the CMDGS mode shows an enhanced gas-sensing sensitivity.

Take the detection of 25 ppm acetone gas as an example, the CMDGS-mode sensor (*i.e.*, the 40-nm-length sample) has a current decrease of about 58% ($1 - I_t/I_0 = 0.58$) while the CDDGS-mode sensor (*i.e.*, the 340-nm-length sample) shows a current increase of about 13% ($I_t/I_0 - 1 = 0.13$), indicating that the sensitivity of CMDGS-mode is more than 4-times higher than that of CDDGS. A similar gas sensing behavior changing from CDDGS to CMDGS exists in detections of the other two reducing gases (ethanol and isopropanol). However, a changing point from CDDGS to CMDGS referring to nanorod length is not in the same range for different gases (Figure 3a-d): the changing point of acetone, isopropanol, and ethanol shall be in the ranges of 340-140 nm, 140-110 nm, and 110-40 nm, respectively. To further investigate the CDDGS-CMDGS changing related to the nanorod length, an 80-nm-length and a 20-nm-length SnO_2 nanorod array are prepared, and 25 ppm ethanol gas is selected as a target gas (see Supporting Information S11). Both the 80-nm-length and the 20-nm-length samples exhibit a negative gas-sensing response, showing a typical CMDGS mode. Figure 3e portrays a correlation of the gas-sensing mode (characterized by $I_t/I_0 > 1$ for CDDGS, or $I_t/I_0 < 1$ for CMDGS) with the nanorod length. Changing from 340 to 110 nm of nanorod length, the sample responses keep positive but their I_t/I_0 value decreases from 1.08 to 1.05. Next the sample exhibits the negative response when its nanorod length decreases to 80 nm, of which I_t/I_0 value is equal to 0.85. The gas-sensing response stays in the negative with the further decreasing of the nanorod length down to the 20 nm. The change from the positive to the negative response occurs when the nanorod length decreases from 110 to 80 nm, indicating that the CDDGS-CMDGS changing point of nanorod length for ethanol is located within the range of 110-80 nm.

As indicated in Figure 3e, the CMDGS is more dominated with the deceasing of nanorod length from 80 to 40 nm. However, with the further decreasing of length from 40 to 20 nm, the

CMDGS dominating becomes weaker. To understand this mechanism, we estimate the scattering length of adsorbed ethanol gaseous molecules on SnO_2. Similar to the close relation of Debye length to gas sensing of adsorbed oxygen molecules on SnO_2,[13] the scattering length of adsorbed ethanol molecules shall play an important role for gas-sensing. For a certain gaseous molecule adsorbed on the surface of SnO_2 nanorod, when its scattering length is large enough to reach the bottom film, it shall influence the carrier mobility in the film and hence cause the CMDGS. In the case of ethanol, the CDDGS mode exists for 110-nm-length sample and turns to the CMDGS when the nanorod length decreases to 80 nm, suggesting that the scattering length of ethanol molecules could be in the range of 80-110 nm. For the 40-nm-length nanorods on a 40-nm-thickness bottom film, all the adsorbed molecules with scattering lengths (80-110 nm) shall be capable of influencing the carriers in the bottom film, and hence contributing to the degradation of carrier mobility and generating a distinct CMDGS. However, the further shortening of nanorods would also decrease the overall number of the adsorbed molecules which leads to a degraded capability to influence the carrier mobility, like the case of the 20-nm-length sample with a reverse trend of the CMDGS. Therefore, an optimum length of nanorods is achievable for obtaining the best CMDGS response, such as 40 nm of nanorod length as the best value for ethanol.

For the sake of further practical applications, detection limitation and long-term stability of CMDGS need to be studied. The 40-nm-length SnO_2 nanorod array, a typical CMDGS-mode gas-sensor, is served as a model gas-sensor. In the study on the detection limit at room temperature, different concentrations of ethanol gases (18, 12, 6, and 3 ppm) are introduced. Then the 40-nm-length SnO_2 nanorod array exhibits corresponding I_t/I_0 of 0.849, 0.921, 0.974, and 0.988 (Figure 3f). This concentration-dependent sensitivity indicates that CMDGS of 40-nm-

length nanorod array has a low detection limit of 3 ppm ethanol gas at room temperature. This ethanol-detection limit of the SnO_2 nanorod array is competitive as compared with those of other SnO_2 gas-sensors. For example, 3D hierarchical SnO_2 nanorods,[26] hierarchical SnO_2 nanostructures,[27] and SnO_2 particles[28] had low detection limits of 1 ppm, 5 ppm, and 1.7 ppm, respectively. However, these reported SnO_2 gas-sensors needed a high operating temperature (> 200 ºC), which impedes their room-temperature applications. Our gas sensors under the CMDGS mode provide a room-temperature application capability. Additionally, the 40-nm-length SnO_2 nanorod array exhibits a high long-term stability (the inset in Figure 3f). After the sensor experiences all the tests shown in Figure 3f and is placed in ordinary surrounding for more than 6 months without any protections, it still exhibits nearly the same sensitivity as that when it is first used in detecting different concentrations of ethanol gases. In detections of 3, 6, 12, and 18 ppm ethanol gases, the 40-nm sample after more than 6 months holds the sensitivities of 0.99, 0.97, 0.92, and 0.84, which are closely similar to the original (*i.e.*, 0.98, 0.97,0.92, 0.85). These results confirm that the 40-nm-length SnO_2 nanorod array is of a high long-term stability in a 6-month measurement.

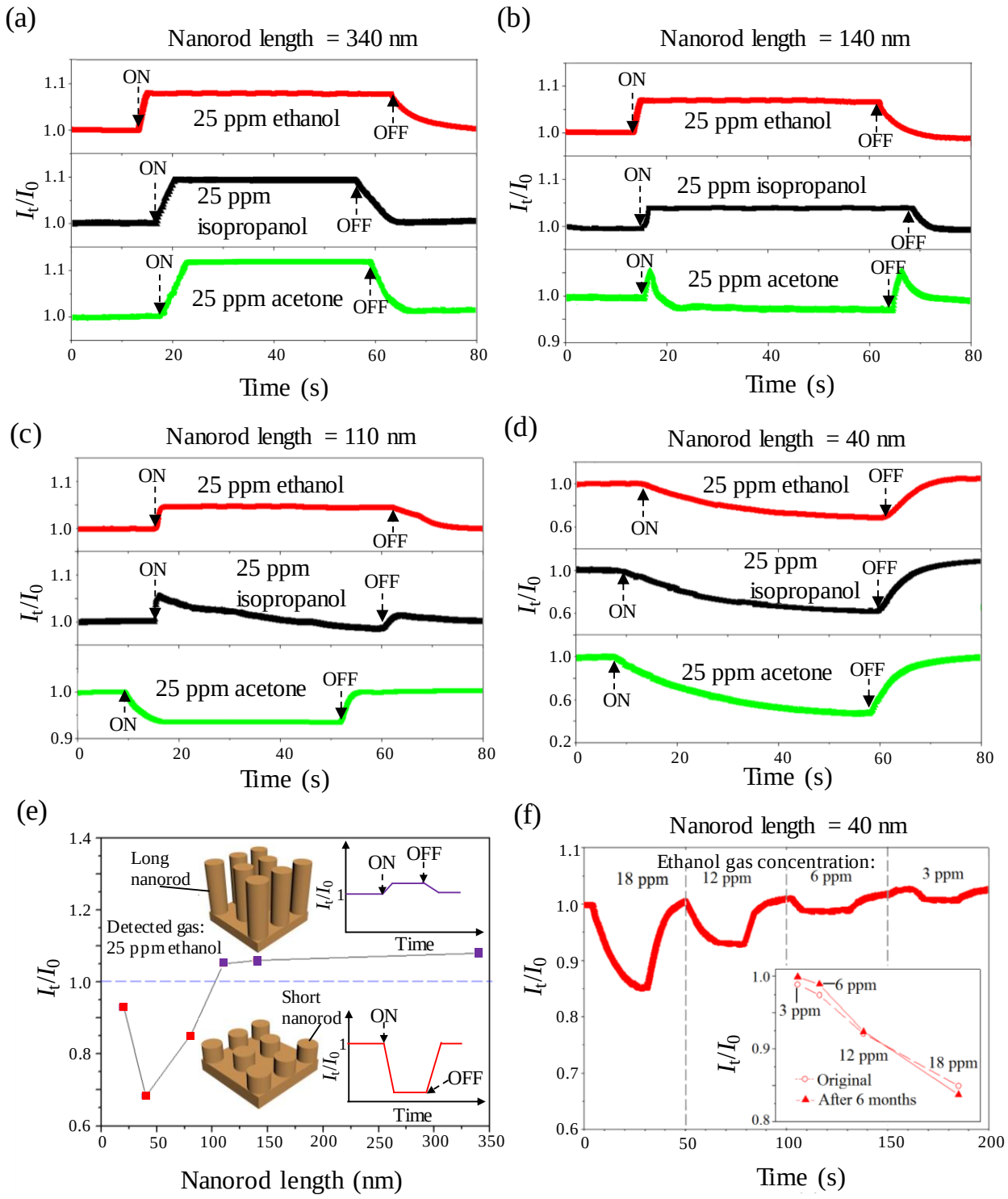

Figure 3. Gas-sensing characteristics of SnO_2 nanorod array gas-sensors. (a-d) Gas-sensing responses to 25 ppm of ethanol, isopropanol, and acetone gases at room temperature versus time

for the SnO_2 nanorod arrays with different nanorod lengths, such as 340 nm (a), 140 nm (b), 110 nm (c), and 40 nm (d). A voltage of 4 V is applied to a device. As the nanorod length decreases from 340 to 40 nm, all sensing responses vary from the positive ($I_t/I_0 > 1$) to the negative ($I_t/I_0 < 1$). (e) The I_t/I_0 of the SnO_2 nanorod array gas-sensor versus the nanorod length (340, 140, 110, 80, 40, and 20 nm) in the detection of 25 ppm ethanol gas, describing that the CMDGS (*i.e.*, $I_t/I_0 < 1$) substitutes the CDDGS (*i.e.*, $I_t/I_0 > 1$) as the nanorod length is shorter than or equal to 80 nm. (f) Gas-sensing responses to 18, 12, 6, and 3 ppm of ethanol gases at room temperature versus time for the 40-nm-length SnO_2 nanorod array. The inset compares the original I_t/I_0 of the 40 nm one with that after 6 months.

3.4. The adsorption-induced degradation of carrier mobility in SnO_2 nanorod arrays. To demonstrate a large adsorption-induced degradation of carrier mobility in the CMDGS of the 40-nm-length SnO_2 nanorod array, the simulation of electric field is firstly performed on two representative SnO_2 nanorod arrays (*i.e.*, the 340-nm-length and the 40-nm-length SnO_2 nanorod array). Figure 4a and b display their electric field strengths on two desirable areas: (i) the bottom film surface and (ii) the interface between nanorods and the bottom film. It is shown that, on the interface between nanorods and the bottom film, the lowest electric field strength of the 40 nm sample (0.27×10^6 V/m) is larger than that of the 340 nm (0.21×10^6 V/m). The stronger electric field strength suggests that the adsorption on the 40-nm-length nanorods might produce a more obvious carrier scattering on the bottom film than that of 340-nm-length nanorods, resulting in a larger carrier mobility degradation in the 40-nm-length nanorod array.

Field-effect transistor characterizations, a well-accepted way to the investigation of carrier mobility,[3] is used to reveal the carrier mobility variation of the SnO_2 nanorod arrays after the introductions of reducing gases. The 40-nm-length and the 340-nm-length SnO_2 nanorod array

are fabricated into field-effect transistors. Two 50-nm-thick Pt electrodes are respectively served as a source and a drain metal contact. The underlying SiO_2 and the p-doped Si substrate are used as a gate dielectric and a gate contact, respectively. Figure 4c and d depict I_{ds}-V_{ds} characteristics of the 340-nm-length (Figure 4c) and the 40-nm-length SnO_2 nanorod array (Figure 4d) measured in reducing gas atmospheres (25 ppm of ethanol, isopropanol and acetone) and air at room temperature. Among them, I_{ds} and V_{ds} are drain-to-source current and voltage, respectively. V_g is the gate voltage and equals to 0 V. It is shown that, as the V_{ds} sweeps from 0 to 5 V, the I_{ds} intensity in air is larger than those exposed to reducing gases for the 40-nm-length SnO_2 nanorod array, while that of the 340-nm-length is reverse. This comparison reveals that the conductivity of the 40-nm-length nanorod array decreases after the introduction of reducing gases.[29]

In order to measure whether the electron mobility (*i.e.*, carrier-mobility) of the 40-nm-length SnO_2 nanorod array decreased in the adsorption-induced conductivity reduction or not, I_{ds}-V_g transfer curves of the 40-nm-length SnO_2 nanorod array in different detected atmospheres are measured at V_{ds} = 4 V as compared to that of the 340 nm. It is found that, an I_{ds}-V_g hysteresis in reducing gases is large for the 40-nm-length nanorod array, indicating its electron mobility should have a distinct variation when the detected atmosphere turns from air to reducing gases.[30] Herein the variation of the electron mobility is defined as $(\mu_r - \mu_{air})/\mu_{air}$. μ_r and μ_{air} are the electron mobilities in the reducing gas and air, respectively. The electron mobility (μ) can be estimated using the following expression, Equation 1:[3]

$$\mu = \left(\frac{dI_{ds}}{dV_g}\right) \times \left(\frac{L^2}{C_{ox}}\right) \times \left(\frac{1}{V_{ds}}\right) \quad (1)$$

where dI_{ds}/dV_g is the transconductance extracted from the linear region of the I_{ds}-V_g curve, L is the distance between two neighboring electrodes. As the nanorod array has a regular geometry and a much larger size (1.2×10^4 μm^2) than the dielectric layer thickness (300 nm), the capacitance (C_{ox}) of the nanorod array with respect to the p++ gate (*i.e.*, the Si substrate) can be approximated as a capacitance between two parallel plates. Combined with the Equation 1, the variation of the electron mobility can be calculated by the Equation 2 as follow:

$$\frac{\mu_r - \mu_{air}}{\mu_{air}} = \frac{\frac{dI_{ds-r}}{dV_{g-r}} - \frac{dI_{ds-a}}{dV_{g-a}}}{\frac{dI_{ds-a}}{dV_{g-a}}} \quad (2)$$

where $dI_{ds\text{-}r}/dV_{g\text{-}r}$ and $dI_{ds\text{-}a}/dV_{g\text{-}a}$ are the transconductances of the I_{ds}-V_g curves in reducing gas and air, respectively. Then the electron mobility of the 40-nm-length nanorod array is estimated to decrease 92.7, 98.9, and 99.9% after introductions of 25 ppm of ethanol, isopropanol, and acetone gases. These more than 90% degradations of the carrier mobility prove a large adsorption-induced degradation of carrier mobility in the CMDGS of the 40-nm-length SnO_2 nanorod array. Furthermore, it is confirmed that the large surface area introduced by 40-nm-length nanorods facilitates an enhanced degradation of electron mobility as compared with that of the flat film (see Supporting Information S12).

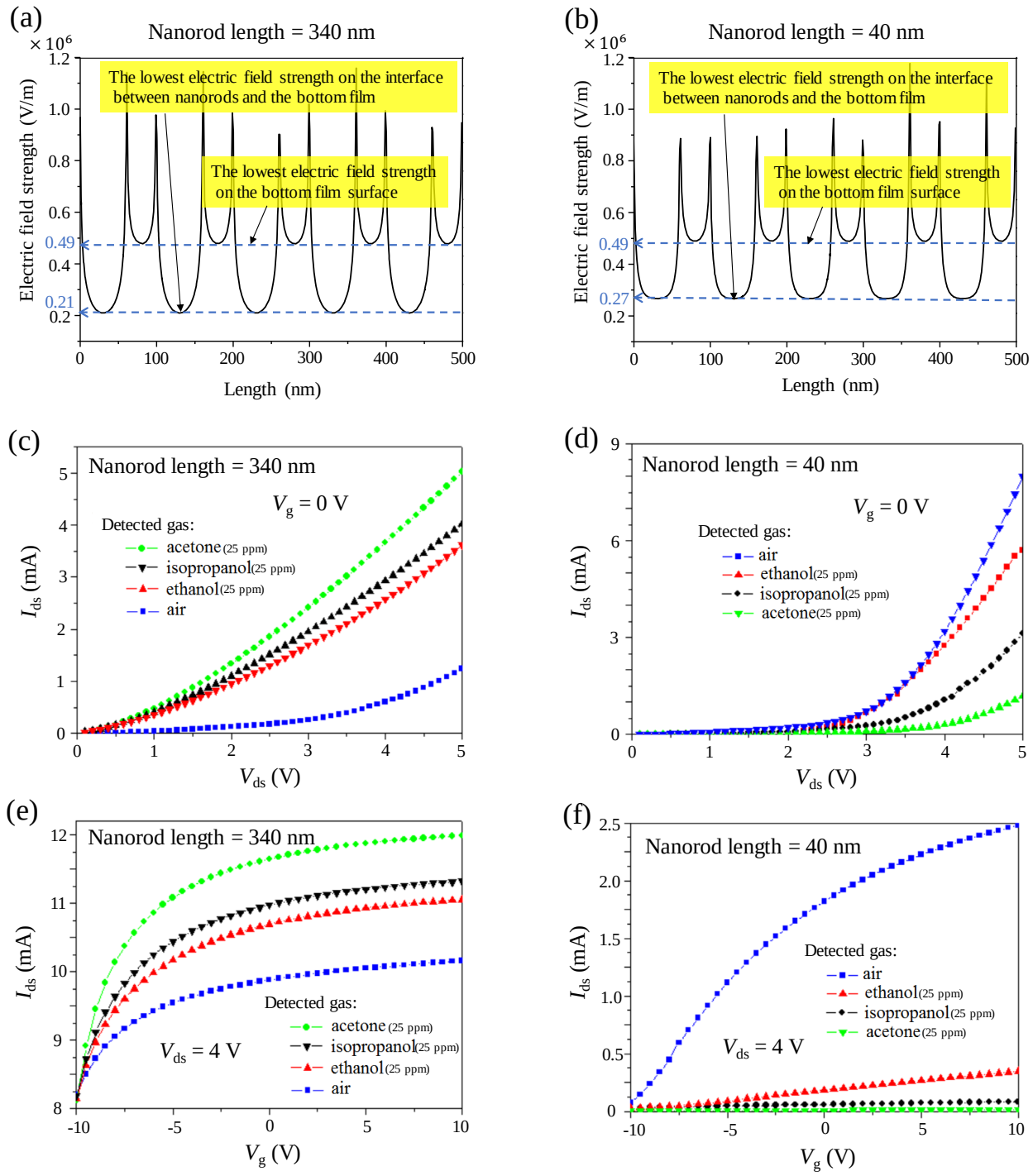

Figure 4. Electric characteristics of SnO_2 nanorod arrays. (a and b) Electric field strengths on two desirable areas of the 340-nm-length (a) and the 40-nm-length nanorod array (b) in air: (i) the bottom film surface and (ii) the interface between nanorods and the bottom film. (c and d) I_{ds}-

V_{ds} curves of the 340-nm-length (c) and the 40-nm-length SnO_2 nanorod array (d) obtained at different detected atmospheres, at room temperature, and $V_g = 0$ V. (e and f) I_{ds}-V_g transfer curves of the 340-nm-length (e) and the 40-nm-length SnO_2 nanorod array (f) at different detected atmospheres, at room temperature, and $V_{ds} = 4$ V.

4. CONCLUSIONS

In summary, we indicate a different gas-sensing mode of CMDGS from the conventional CDDGS mode for inorganic semiconductor gas-sensors. To demonstrate this CMDGS, we firstly design and fabricate a regular array of SnO_2 nanorods on a bottom film, then use it for room temperature gas-sensing. By modulating the length of arrayed nanorods, the gas-sensing behavior changes from CDDGS to a complete CMDGS mode. Moreover, the realized CMDGS-mode gas-sensor is of a more than 4-times higher sensitivity than that of the CDDGS-mode. It is anticipated that the proposed CMDGS mode shall be applicable to other gas sensing systems of different inorganic semiconductors, providing a concept for designing gas-sensors.

ASSOCIATED CONTENT

Supporting Information.

The Supporting Information is available free of charge.

S1. Electric field strengths on the bottom film surface of the nanorod array; S2. The morphology of an UTAM; S3. The configuration of a gas-sensor; S4. The composition of a SnO_2 nanorod array; S5. Electron trapping of adsorbed oxygen molecules on SnO_2 nanorod arrays; S6. Formation mechanism of SnO_2 nanorod arrays; S7. SnO_2 nanorod arrays prepared by modulating concentration of the precursor solution; S8. Agglomerations of SnO_2 nanorods unconnected with

the bottom film; S9. Output characterizations of SnO_2 nanorod arrays; S10. Gas-sensing properties of the 40-nm-length nanorod arrays with different nanorod diameters; S11. SnO_2 nanorod array gas-sensors with the 80 nm and the 20 nm of nanorod lengths. S12. SnO_2 film gas-sensors with different film thicknesses. (PDF)

AUTHOR INFORMATION

Corresponding Author

* E-mail: yong.lei@tu-ilmenau.de.

Notes

The authors declare no competing financial interest.

ACKNOWLEDGMENT

This work is financially supported by the European Research Council (ThreeDsurface, 240144), European Research Council (HiNaPc, 737616), Federal Ministry of Education and Research in Germany (BMBF, ZIK-3DNanoDevice, 03Z1MN11), German Research Foundation (DFG: LE 2249_4-1), and the China Scholarship Council.

REFERENCES

(1) Baker, A. R.; Firth, J. G. The Estimation of Firedamp: Applications and Limitations of the Pellistor. *Mining Eng. (London)* **1969**, *128*, 237-244.

(2) Liu, X.-H.; Yin, P.-F.; Kulinich, S. A.; Zhou, Y.-Z.; Mao, J.; Ling, T.; Du, X.-W. Arrays of Ultrathin CdS Nanoflakes with High-Energy Surface for Efficient Gas Detection. *ACS Appl. Mater. Interfaces* **2017**, *9*, 602-609.

(3) Pan, X.; Liu, X.; Bermak, A.; Fan, Z. Self-Gating Effect Induced Large Performance Improvement of ZnO Nanocomb Gas Sensors. *ACS Nano* **2013**, *7*, 9318-9324.

(4) Ou, J. Z.; Ge, W.; Carey, B.; Daeneke, T.; Rotbart, A.; Shan, W.; Wang, Y.; Fu, Z.; Chrimes, A. F.; Wlodarski, W.; Russo, S. P.; Li, Y. X.; Kalantar-zadeh, K. Physisorption-Based Charge Transfer in Two-Dimensional SnS_2 for Selective and Reversible NO_2 Gas Sensing. *ACS Nano* **2015**, *9*, 10313-10323.

(5) Cui, S.; Pu, H.; Wells, S. A.; Wen, Z.; Mao, S.; Chang, J.; Hersam, M. C.; Chen, J. Ultrahigh Sensitivity and Layer-Dependent Sensing Performance of Phosphorene-Based Gas Sensors. *Nat. Commun.* **2015**, *6*, 8632-8640.

(6) Barsan, N.; Weimar, U. Conduction Model of Metal Oxide Gas Sensors. *J. Electroceram.* **2001**, *7*, 143-167.

(7) Barsan, N.; Weimar, U. Understanding the Fundamental Principles of Metal Oxide Based Gas Sensors; the Example of CO Sensing with SnO_2 Sensors in the Presence of Humidity. *J. Phys. Condens. Matter* **2003**, *15*, R813-R83.

(8) Gurlo, A.; Riedel, R. In Situ and Operando Spectroscopy for Assessing Mechanisms of Gas Sensing. *Angew. Chem. Int. Ed.* **2007**, *46*, 3826-3848.

(9) Yoo, H.-W.; Cho, S.-Y.; Jeon, H.-J.; Jung, H.-T. Well-Defined and High Resolution Pt Nanowire Arrays for A High Performance Hydrogen Sensor by A Surface Scattering Phenomenon, *Anal. Chem.* **2015**, *87*, 1480-1484.

(10) Yang, F.; Donavan, K. C.; Kung, S.-C.; Penner, R. M. The Surface Scattering-Based Detection of Hydrogen in Air Using A Platinum Nanowire. *Nano Lett*. **2012**, *12*, 2924-2930.

(11) Chandran, G. T.; Li, X.; Ogata, A.; Penner, R. M. Electrically Transduced Sensors Based on Nanomaterials (2012–2016). *Anal. Chem.* **2017**, *89*, 249-275.

(12) Sun, J.; Muruganathan, M.; Mizuta, H. Room Temperature Detection of Individual Molecular Physisorption Using Suspended Bilayer Graphene. *Sci. Adv.* **2015**, *2*, e1501518-1501524.

(13) Ogawa, H.; Nishikawa, M.; Abe, A. Hall Measurement Studies and An Electrical Conduction Model of Tin Oxide Ultrafine Particle Films. *J. Appl. Phys.* **1982**, *53*, 4448-4455.

(14) Cho, I.; Kang, K.; Yang, D.; Yun, J.; Park, I. Localized Liquid-Phase Synthesis of Porous SnO_2 Nanotubes on MEMS Platform for Low-Power, High Performance Gas Sensors. *ACS Appl. Mater. Interfaces* **2017**, *9*, 27111-27119.

(15) Wang, X.; Aroonyadet, N.; Zhang, Y.; Mecklenburg, M.; Fang, X.; Chen, H.; Goo, E.; Zhou, C. Aligned Epitaxial SnO_2 Nanowires on Sapphire: Growth and Device Applications. *Nano Lett.* **2014**, *14*, 3014-3022.

(16) Li, Y.-X.; Guo, Z.; Su, Y.; Jin, X.-B.; Tang, X.-H.; Huang, J.-R.; Huang, X.-J.; Li, M.-Q.; Liu, J.-H. Hierarchical Morphology-Dependent Gas-Sensing Performances of Three-Dimensional SnO_2 Nanostructures. *ACS Sensors* **2017**, *2*, 102-110.

(17) Xu, S.; Sun, F.; Pan, Z.; Huang, C.; Yang, S.; Long, J.; Chen, Y. Reduced Graphene Oxide-Based Ordered Macroporous Films on A Curved Surface: General Fabrication and Application in Gas Sensor. *ACS Appl. Mater. Interfaces* **2016**, *8*, 3428-3437.

(18) Lei, Y.; Chim, W.K.; Sun, H.P.; Wilde, G. Highly Ordered CdS Nanoparticle Arrays on Silicon Substrates and Photoluminescence Properties. *Appl. Phys. Lett.* **2005**, *86*, 103106-103108.

(19) Zhan, Z.B.; Lei, Y. Sub-100-nm Nanoparticle Arrays with Perfect Ordering, Tunable and Uniform Dimensions Fabricated by Combining Nanoimprinting with Ultrathin Alumina Membrane Technique. *ACS Nano* **2014**, *8*, 3862-3868.

(20) Wen, L. Y.; Mi, Y.; Wang, C. L.; Zhao, H. P.; Grote, F.; Zhan, Z. B.; Zhou, M.; Lei, Y. Cost-Effective Atomic Layer Deposition Synthesis of Pt Nanotube Arrays: Application for High Performance Supercapacitor. *Small* **2014**, *10*, 3162-3168.

(21) Wang, S. X.; Wang, M.T.; Lei, Y.; Zhang, L.D. Anchor Effect in Poly(Styrene Maleic Anhydride)/TiO_2 Nanocomposites. *J. Mater. Sci. Lett.* **1999**, *18*, 2009-2012.

(22) Chen, W.; Cai, W. P.; Lei, Y.; Zhang, L. D. A Sonochemical Approach to the Confined Synthesis of Palladium Nanocrystalline within Mesoporous Silica. *Mater. Lett.* **2001**, *50*, 53-56.

(23) Sun, F.; Cai, W.; Li, Y.; Jia, L.; Lu, F. Direct Growth of Mono- and Multilayer Nanostructured Porous Films on Curved Surfaces and Their Application as Gas Sensors. *Adv. Mater.* **2005**, *17*, 2872-2877.

(24) Wang, Y.-T.; Whang, W.-T.; Chen, C.-H. Hollow V_2O_5 Nanoassemblies for High-Performance Room-Temperature Hydrogen Sensors. *ACS Appl. Mater. Interfaces* **2015**, *7*, 8480-8487.

(25) Tricoli, A.; Righettoni, M.; Teleki, A. Semiconductor Gas Sensors: Dry Synthesis and Application. *Angew. Chem. Int. Ed.* **2010**, *49*, 7632-7659.

(26) Liu, Q.; Zhang, Z.; Li, W.; Xu, K.; Zou, R.; Hu, J. Ethanol Gas Sensor Based on A Self-Supporting Hierarchical SnO_2 Nanorods Array. *CrystEngComm* **2015**, *17*, 1800-1804.

(27) Liu, Y.; Jiao, Y.; Zhang, Z.; Qu, F.; Umar, A.; Wu, X. Hierarchical SnO_2 Nanostructures Made of Intermingled Ultrathin Nanosheets for Environmental Remediation, Smart Gas Sensor, and Supercapacitor Applications. *ACS Appl. Mater. Interfaces* **2014**, *6*, 2174-2184.

(28) Chiu, H.-C.; Yeh, C.-S. Hydrothermal Synthesis of SnO_2 Nanoparticles and Their Gas-Sensing of Alcohol. *J. Phys. Chem. C* **2007**, *111*, 7256-7259.

(29) Zou, X.; Wang, J.; Liu, X.; Wang, C.; Jiang, Y.; Wang, Y.; Xiao, X.; Ho, J. C; Li, J.; Jiang, C.; Fang, Y.; Liu, W.; Liao, L. Rational Design of Sub-Parts per Million Specific Gas Sensors Array Based on Metal Nanoparticles Decorated Nanowire Enhancement-Mode Transistors. *Nano Lett.* **2013**, *13*, 3287-3292.

(30) Yun, S. J.; Chae, S. H.; Kim, H.; Park, J. C.; Park, J.-H.; Han, G. H.; Lee, J. S.; Kim, S. M.; Oh, H. M.; Seok, J.; Jeong, M. S.; Kim, K. K.; Lee, Y. H. Synthesis of Centimeter-Scale Monolayer Tungsten Disulfide Film on Gold Foils. *ACS Nano* **2015**, *9*, 5510-5519.